Capacitive Sensing for Measuring the Conduction Zone of Low Density PETN

James Edgeley and Chris Braithwaite

Surfaces, Microstructure and Fracture Group, Department of Physics, University of Cambridge.

(*Electronic mail: chb32@cam.ac.uk.)

(Dated: 5 December 2022)

We present a novel diagnostic system, based on the the principle of capacitive sensing, capable of detecting the conduction zone of detonating explosives. The method relies on measuring the change in the capacitive coupling between a printed circuit and its surroundings, induced by an increase in local conductivity. A high frequency wave generator provides the driving signal which is modified by the change in coupling. This method boasts a greater sensitivity than existing conductivity-based techniques, with comparable resolution. The subject material was pentaerythritol tetranitrate (PETN) powder, pressed into low density (50 % to 85 %) theoretical maximum density (TMD) cylindrical columns. Previous attempts to measure the reaction zone of low density PETN have faced difficulties because of its short length and low conductivity compared to other explosives. The PETN was initiated using a laser flyer detonator in order to reach detonation promptly and with a minimum of electrical noise. Application of the capacitive sensor diagnostic and subsequent analysis yielded a density dependent steady-state reaction zone length of between 45 μm and 78 μm.

I. INTRODUCTION

Measuring the reaction zone of a detonating explosive is a challenging undertaking – this transient region generally spans less than a millimetre, moves at several kilometres per second, and is accompanied by a shock destructive to most things it encounters. One canonical method is to measure the change in electrical conductivity that occurs from the unreacted explosive to the products, via the intermediate reaction zone[1]. Typically these conductivity measurements[2,3] use a coaxial electrode and a high voltage ($\sim 1\,\text{kV}$), which causes a current to flow in the reaction zone. Time-resolved measurements of the current or voltage drop, depending on the exact technique, then inform the nature of the conductivity profile. These contact methods, where there is a direct flow of current between the electrode and explosive, are sensitive to distortions due to the high voltage. Other authors[4,5] have used interferometric methods (Fabry-Pérot, VISAR) to infer the properties of the reaction zone transferred to a reflective foil layer – however these make assumptions about the constancy of the detonation velocity.

The method presented here does not directly measure conductivity, but the changes to the transfer function of a sensor circuit. In this way the need for a high voltage and any potential distortion is avoided. This technique is only now possible due to improvements in instrument bandwidth, allowing a signal frequency high enough to reach the requisite temporal resolution. Unlike the optical methods, it is possible to measure the detonation velocity and reaction zone directly at several points within a single experiment.

The theoretical background of capacitive sensing is discussed, and our implementation described in Section II. Capacitive sensing was applied to low density PETN, an explosive with a short and relatively low conductance reaction zone – Section III gives details of these experiments. The results are presented in Section IV, along with a discussion of the observed trends. Section VI summarises our conclusions for the experimental work and future applications of the technique.

II. CAPACITIVE SENSORS

The underlying principle of the diagnostic we have developed is that small changes to the conductance of the local environs of a sensing circuit will modify its response to a high frequency signal via capacitive coupling. The design of the circuit affects the size of the change in response, and therefore the sensitivity of the technique. Spatial resolution is determined by the size of features on the printed circuit, while temporal resolution is limited by the signal frequency and oscilloscope bandwidth. The inherent high sensitivity means that noise is a concern – several features of the sensor are intended to help mitigate its magnitude. Capacitive sensing has been applied at a microscopic scale in other fields[6,7], although not at such a high rate. Unlike these other applications which use dedicated demodulation and amplification hardware, processing of the raw data was performed post-experiment using software. While the premise is simple, there are several analysis steps to perform in order to condense the raw data to useful information.

A. Capacitive Coupling

The transfer function is the property of an electrical network which describes the mapping of an input signal to an output. In general this mapping involves changes in the phase and amplitude of each frequency component in the original signal. The transfer function for input signal $u(t)$ to output signal $v(t)$ is given by:

$$H(s) = \frac{V(s)}{U(s)} = \frac{\mathscr{L}\{v(t)\}}{\mathscr{L}\{u(t)\}} \tag{1}$$

where $X(s) = \mathscr{L}\{x(t)\}$ denotes the Laplace transform (reduces to the Fourier transform with conjugate variable ω in non-transient applications such as here). In a generalised RLC circuit the transfer function will be a func-
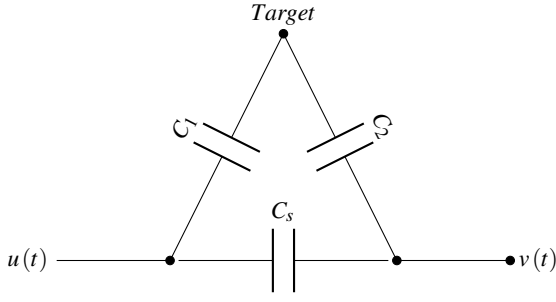
FIG. 1. The capacitive sensor can be represented by an equivalent circuit. When a target is detected the transfer function changes to include C_1 and C_2 as well as the original sensor capacitance C_S.
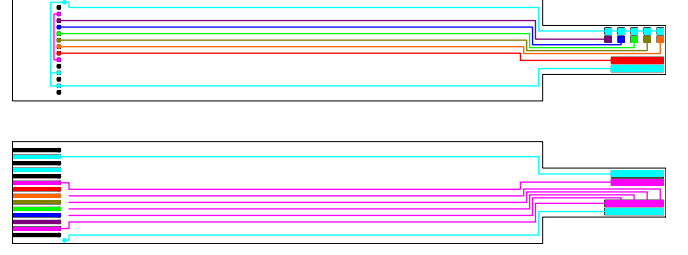

FIG. 2. The front layer of the sensor contains the individual channel receiver electrodes (five short and one long), while the back layer contains the shared transmitter electrodes and 14 connection pads. For clarity each electrical net is a different colour: Channel 1, Channel 2, Channel 3, Channel 4, Channel 5, Channel 6, Transmitter, Shield, Ground.

tion of the impedances of each component: $H\left(\omega; R_i, L_i, C_i\right)$. Changing either the frequency, or any of the components' impedance therefore changes the transfer function. An input signal containing different frequency components will therefore also change shape as well as size in response to impedance changes.

Capacitive coupling occurs when a circuit is in proximity to an electrical conductor. Additional capacitance appears between the circuit and target, modifying the transfer function. A simple equivalent circuit which demonstrates this effect is shown in Fig. 1.

The degree to which the transfer function changes depends on the degree of capacitive coupling. Therefore the change in the output signal compared to the uncoupled circuit will indicate the proximity and conductivity of the target.

B. Implementation

Our capacitive sensing system uses a multi-channel approach to detect the degree of capacitive coupling to the reaction zone at several points along the path of a detonation wave. Although they share the input signal, each channel has an independent output signal, and so produces a similar but lagged signal to the previous channel. Combining the data from each channel gives a more complete picture of the evolution of the reaction zone.

The important components of our implementation of the capacitive sensing diagnostic are as follows:

1. An arbitrary waveform generator (Tektronix AWG70002A), which produces the pulse train which composes the input signal,

2. The sensor is a flexible printed circuit (FPC) containing transmitter, receiver and shield electrodes.

3. A high bandwidth oscilloscope (Tektronix DPO7254) to receive and record the output signal.

4. A junction box connecting the other components together with coaxial cables.

While in theory any waveform would work for the input signal, a square wave was chosen due to its shape – a square

wave contains multiple frequencies, and therefore changes both shape and amplitude when filtered by an RC circuit. The data processing method relies on calculating the misfit of the output signal compared to a baseline so the best waveform is one which changes significantly in response to small changes in the transfer function.

The oscilloscope has a bandwidth of 2.5 GHz, which puts a soft upper bound on the signal frequency of 500 MHz (using the general rule of thumb that an oscilloscope should have a bandwidth 5 higher than the fundamental frequency it measures[8]). With all four channels in use, the sampling rate is 10 GS/s, therefore 20 voltage measurements are made for each signal period. The oscilloscope record window is triggered by a TTL signal from the delay generator in order to synchronise with the detonator.

1. Sensors

The sensors themselves are double layer flexible printed circuits produced by P. W. Circuits. There is a layer of 65 μm thick copper etched on each side of 25 μm thick polyimide by a photolithographic process. The sensor has six channels; each channel consists of a transmitter electrode, a receiver electrode and a pair of shield electrodes. The five short 0.5 mm × 0.5 mm channels share a transmitter electrode, while the adjacent long 0.5 mm × 4 mm channel has its own transmitter electrodes. Both transmitter electrodes are connected to the same input source. Each channel also has a pair of adjacent active shielding electrodes (explained below); the five short channels also share one shielding pair.

The electrodes in the sensor head are connected to the pads via 0.1 mm wide tracks and 0.1 mm diameter plated through holes (PTH). The tracks are approximately 4 cm long: any shorter and it would risk more components needing to be replaced after each shot; any further and the tracks' own capacitance would become influential. The two copper layers of the PCB are shown in Fig. 2.

The head section of the sensor containing the electrodes is inserted into a charge of explosive. The tail of the sensor inserts into a 14 pin FPC connector mounted on the junction box. The junction box connects the transmitter and shield sig-
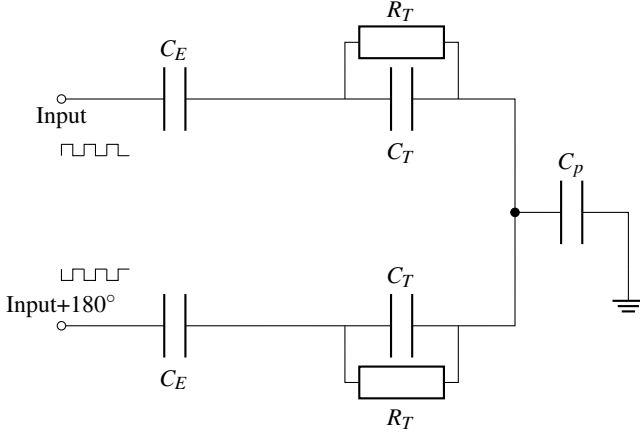
FIG. 3. By making the shield electrodes symmetric to the sensing electrodes, the voltage across parasitic capacitance is approximately constant, limiting the effect the parasitic capacitance has on the signal.

nals from the AWG to the corresponding sensor electrodes, and the receiver electrodes to separate channels on the oscilloscope using coaxial cables (Thorlabs CA2948).

2. Active Shielding

In order to maximise the signal-to-noise ratio (SNR) of the sensors it is necessary to maximise their capacitive coupling to the reaction zone, while minimising coupling to other objects. A technique known as active shielding is used to reduce this unwanted interference[9].

The shielding channels carry a signal of the same magnitude and shape as that sent to the transmitter electrode, but $180°$ out of phase. In this way, the voltage at the centre of symmetry is constant, as therefore is the voltage difference across the stray (parasitic) capacitance (see Fig. 3). This destructive interference prevents the parasitic capacitance from contributing to the output signal.

This out-of-phase technique only works for stray capacitances that enter between the shield and sensing electrodes. It is still important to reduce other interferences, which is done by using coaxial cables to connect the sensor to the instruments, and within the junction box. The active shielding also improves the focus of the sensing zone on the area of interest, therefore reducing the edge effects – these are considered in more detail below. The wave generator has a positive and negative output which have equal and opposite potential at all times. These outputs were connected to the transmitter and shield electrodes of the sensor.

C. Data Processing

The raw data consists of the unaltered baseline signal, followed by the region of interest, followed by junk data after the detonation has completed and the sensor destroyed. The first step in data processing is to manually identify a region of the signal before initiation to use as the baseline. This baseline time series $g_b(t)$ is then extended forward in time by t_b such that it remains in phase with the unshifted version of itself, and its extent covers the region of interest. It is then left to calculate the time-varying degree of 'difference' between the extended baseline and the whole signal. Using the algebraic difference between the two is insufficient, since this drops to zero when the two signals cross. A more complex analysis is required that reflects the possibility that both the phase and spectral composition could change. Instead they are compared by performing a continuous wavelet transformation to both series and calculating misfit functions.

1. Continuous Wavelet Transform

The continuous wavelet transform[10] is a conversion of the pure time-domain signal into a mixed frequency-time representation that falls between the original signal and the Fourier transform. The transform is performed by convolving the time series $g(t)$ with a series of wavelet functions $\psi(t)$ scaled by the frequency f.

$$W(t,f) = \sqrt{\frac{2\pi |f|}{\omega_0}} \int_{-\infty}^{\infty} g(\tau)\psi^*\left(2\pi f \frac{\tau - t}{\omega_0}\right) d\tau \quad (2)$$

Intuitively, the CWT represents the different contributions to a signal from wavelets with different amounts of scaling (by the frequency parameter f) and translation (by the time parameter t). A suitable wavelet function that obeys the mathematical criteria for the CWT is the Morlet wavelet:

$$\psi(t) = \frac{1}{\pi^{\frac{1}{4}}} e^{i\omega_0 t} e^{-\frac{t^2}{2}} \quad (3)$$

This function is a complex exponential bounded by a Gaussian − ω_0 sets the number of oscillations that fit under the Gaussian envelope. The Morlet wavelet is shown in Fig. 4.

2. Signal Misfit

From the CW transformed baseline and main signals, the 'misfit' functions of Kristeková, Kristek, and Moczo[11] are used to evaluate the phase and amplitude difference. The amplitude misfit M_A is:

$$M_A(t,f) = \frac{|W(t,f)| - |W_b(t,f)|}{|W_b(t,f)|} \quad (4)$$

and the phase misfit M_ϕ is:

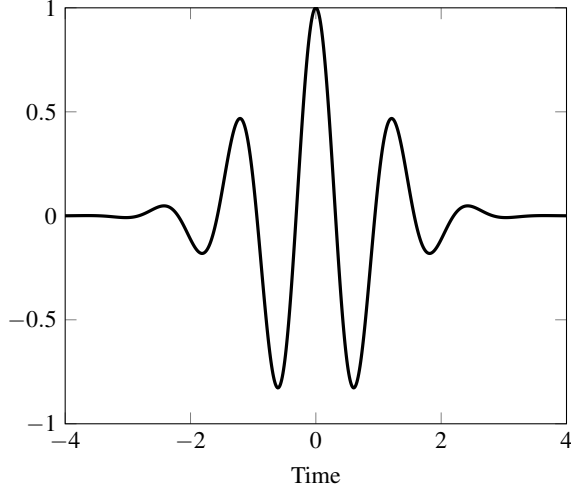$$M_\phi(t,f) = \frac{1}{\pi} Arg\left(\frac{W(t,f)}{W_b(t,f)}\right) \quad (5)$$

FIG. 4. The Morlet wavelet.

FIG. 5. The misfit signal from the ith electrode starts to rise when the front edge of the reaction zone crosses into its sensing zone (α) and levels off when the rear edge crosses into it (β). It starts to fall when the front edge of the reaction zone crosses out of the electrode's sensing zone (γ) and finishes falling when the rear edge of the reaction zone crosses out of it (δ). Since the reaction zone has not entered the $(i+1)^{th}$ electrode's sensing zone by this point, the traces are separated.

This technique encompasses both phase and amplitude/envelope information, which can be conveyed in a two-dimensional $t - f$ plane. Individually they can be conveyed as one-dimensional time series by summing over the frequency:

$$M_A(t) = \frac{\sum_f |W_b(t,f)| M_A(t,f)}{\sum_f |W_b(t,f)|} \qquad (6)$$

$$M_\phi(t) = \frac{\sum_f |W_b(t,f)| M_\phi(t,f)}{\sum_f |W_b(t,f)|} \qquad (7)$$

Since the baseline signal differs between channels, in order to make meaningful comparisons between channels, the misfit is normalised by the envelope of the baseline analytic signal $\sum_f |W_b(t,f)|$. This local definition means that the misfit at a particular time can be determined using only data at that time.

FIG. 6. Idealised trace for a reaction zone shorter than 0.5 mm that becomes shorter and stronger over the course of the detonation. The peaks for each channel are completely separate.

D. Data Analysis

The processed data represents the shift in capacitive coupling that occurs when the conduction zone passes over an electrode of the sensor. Deconvolving the processed signal with the shape of the electrode's sensing zone yields the shape of the reaction zone conductivity profile. The following analysis assumes the reaction zone length ξ is shorter than the width $w = 0.5$ mm, and therefore only interacts with one electrode at a time. A typical sequence of events arising from such a reaction zone is shown in Fig. 5 and the resulting trace shown in Fig. 6.

The positions of the detonation front and sonic locus over time can be used to determine their velocities and the reaction zone length as shown below.
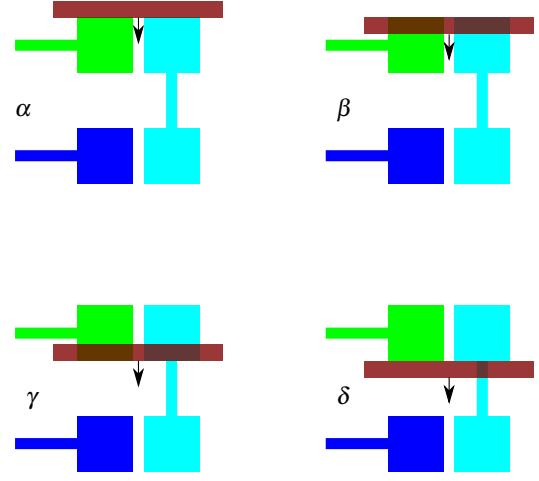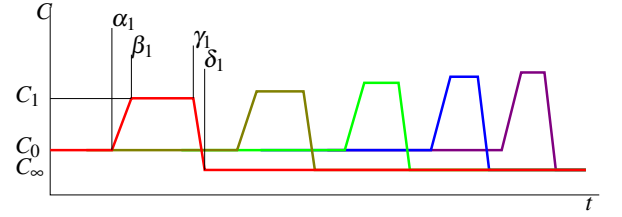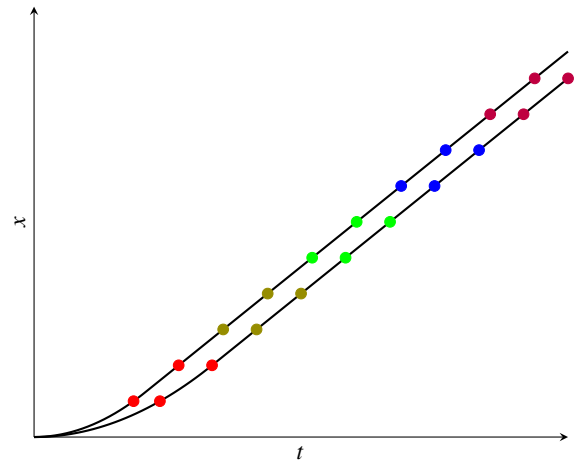

FIG. 7. Illustration of how the timing points $\alpha_i, \beta_i, \gamma_i, \delta_i$ can be used to give a displacement-time graph for the detonation front (top branch) and sonic locus (bottom branch).

1. Detonation Velocity

For this analysis the detonation velocity is considered to be the velocity of the front edge of the reaction zone. There are two ways that this can be obtained from the traces. The detonation velocity across the electrode can be calculated from the time between the front entering the electrode's sensing zone and leaving it. Interpolating to the centre of the electrode gives:

$$D_i = \frac{w}{\gamma_i - \alpha_i} \tag{8}$$

The detonation velocity in the gap between two adjacent electrodes can be calculated from the time between the front leaving one electrode's sensing zone and entering another's. Interpolating to the midpoint between the two electrodes gives:

$$D_{i+\frac{1}{2}} = \frac{w}{\alpha_{i+1} - \gamma_i} \tag{9}$$

2. Chapman-Jouguet Velocity

The Chapman-Jouguet velocity is here taken to be the velocity of the rear of the reaction zone. In the same way as with the detonation velocity, it can be calculated from the time between the rear of the conduction zone entering the sensing zone and leaving it:

$$V_i = \frac{w}{\delta_i - \beta_i} \tag{10}$$

Likewise, between electrodes it is:

$$V_{i+\frac{1}{2}} = \frac{w}{\beta_{i+1} - \delta_i} \tag{11}$$

3. Reaction Zone Length

At the first timing point α_i, the front of the reaction zone has just entered the sensing zone, and the back of the reaction zone is a distance $\xi_{i-\frac{1}{4}}$ behind and moving at a velocity $V(\alpha_i)$. At time β_i the back edge enters the electrode at velocity $V(\beta_i)$ having travelled the distance $\xi_{i-\frac{1}{4}}$. $\xi_{i-\frac{1}{4}}$ can therefore be expressed as:

$$\xi_{i-\frac{1}{4}} = \int_{\alpha_i}^{\beta_i} V(t)\,dt \tag{12}$$

At the timing point β_i, the rear edge enters the sensing zone and the front edge is a distance $w - \xi_i$ away from leaving, and travelling at $D(\beta_i)$. At time γ_i it leaves at a velocity of $D(\gamma_i)$. Integrating gives ξ_i:

TABLE I. The method of calculating reaction zone properties based on the above analysis. The continuum approximations are made by interpolating the discrete measurements from the sensor's measurement zones.

Property	Discrete Evaluation		Continuum Approximation
Detonation Velocity	D_i	$= \dfrac{w}{\gamma_i - \alpha_i}$	$D(t)$
	$D_{i+\frac{1}{2}}$	$= \dfrac{w}{\alpha_{i+1} - \gamma_i}$	
Rear Velocity	V_i	$= \dfrac{w}{\delta_i - \beta_i}$	$V(t)$
	$V_{i+\frac{1}{2}}$	$= \dfrac{w}{\beta_{i+1} - \delta_i}$	
Reaction Zone Length	$\xi_{i-\frac{1}{4}}$	$= \displaystyle\int_{\alpha_i}^{\beta_i} V(t)\,dt$	$\xi(t)$
	ξ_i	$= w - \displaystyle\int_{\beta_i}^{\gamma_i} D(t)\,dt$	
	$\xi_{i+\frac{1}{4}}$	$= \displaystyle\int_{\gamma_i}^{\delta_i} V(t)\,dt$	
	$\xi_{i+\frac{1}{2}}$	$= w - \displaystyle\int_{\delta_i}^{\alpha_{i+1}} D(t)\,dt$	

$$\xi_i = w - \int_{\beta_i}^{\gamma_i} D(t)\,dt \tag{13}$$

Using the same analysis in the gap between electrodes gives:

$$\xi_{i+\frac{1}{4}} = \int_{\gamma_i}^{\delta_i} V(t)\,dt \tag{14}$$

and:

$$\xi_{i+\frac{1}{2}} = w - \int_{\delta_i}^{\alpha_{i+1}} D(t)\,dt \tag{15}$$

4. Errors

There are two categories of experimental uncertainty in the capacitive sensing apparatus – spatial uncertainty in the position of the sensing elements, and temporal uncertainty in the timing points.

The manufacturing process for the sensors uses a highly accurate photolithographic machine with a tolerance of $\pm 5\,\mu\text{m}$, or $\pm 1\,\%$ of the small electrode width w. The positioning of the sensor in the charge may also reduce the spatial accuracy

if it is inserted at an angle, or is not flush to the surface. By aligning the shoulders of the sensor to be parallel with the face of the charge during insertion, the angular uncertainty can be reduced to approximately $\pm 1°$, corresponding to a spatial uncertainty of around $\pm 17 \mu m$.

The minimum uncertainty in continuous wavelet transforms is determined by the width of the wavelet. For this analysis the temporal uncertainty is taken to be one period of the input signal. For a 500 MHz signal, with a 2 ns time period, the equivalent spatial uncertainty for a steady detonation wave in low density PETN is around $\pm 10 \mu m$.

Furthermore, the oscilloscope has a rise time of 160 ps, so signal rise time accuracy is limited to around five times this, 800 ps.

All together, the errors amount to no more than a few multiples of the particle size. The most important experimental consideration is ensuring that the sensor is glued properly within the charge, and does not become damaged or dislodged during the pressing of the explosive. The sensor can be placed accurately to within $100 \mu m$, but for the differential measurements on which most data are based the manufacturing error of $5 \mu m$ is used.

III. EXPERIMENT

The experimental apparatus consisted of the capacitive sensing diagnostic described above, synchronised to a laser flyer detonator. The sensors were attached to PMMA casings, into which columns of PETN were pressed.

A. Laser Detonator

The PETN was initiated using a fibre-coupled laser flyer detonator (shown in Fig. 8). The laser used was a Big Sky/Quantel CFR (Compact Folded Resonator) 400 mJ Q-switched Nd:YAG lamp pumped pulsed laser operating at 1064 nm. A diode laser and fiducial fibre aided in alignment of the optical components. Neutral density (ND) filters attenuate the pulse energy to avoid optical damage to the fibre, while a half-wave plate and polarising beam splitter allow fine-control variation. A lens tube containing two lenses sandwiching a microlens array homogenises and focuses the beam into a $550 \mu m$ diameter high power fibre, which is aligned with a 5-axis stage.

At the output end of the fibre, the beam is incident on the coated flyer substrates as shown in Fig. 9. The output face of the fibre was polished between each experiment in order to avoid accumulation of surface damage.

The system can launch flyers at velocities of $5 \, km \, s^{-1}$, as measured by streak photography.

B. Target

In order to obtain accurate data, it is important that the sensor is well aligned within the cylindrical PMMA casing before
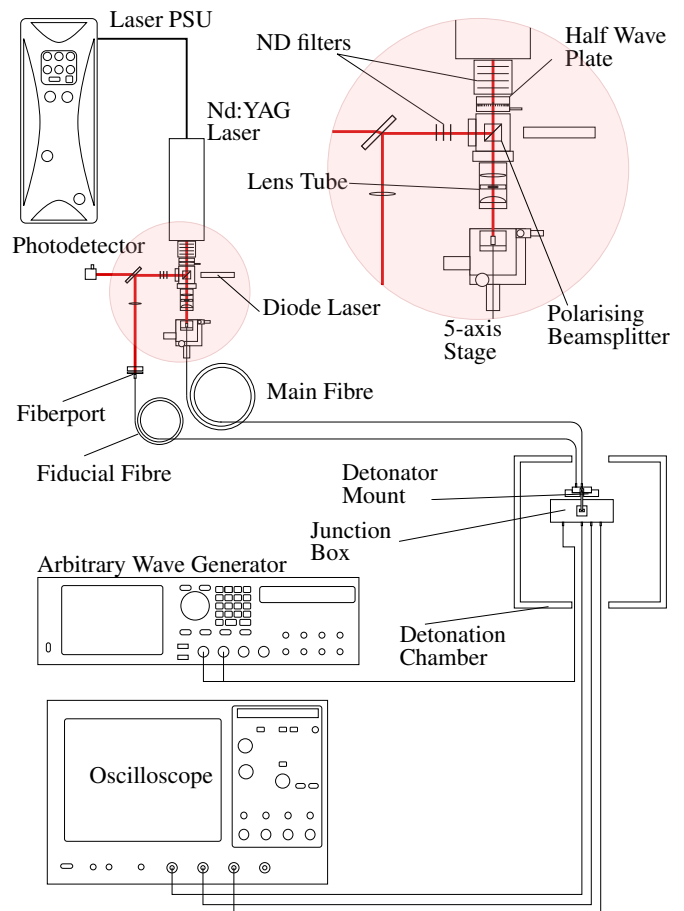

FIG. 8. The experimental apparatus including the laser detonator and capacitive sensing system. Not shown is the delay generator which synchronises the detonator and diagnostics.

being glued in place as shown in Fig. 10. The alignment was performed with the use of fixed mount and a back-illuminated magnifying lens. With careful placement it was possible to reduce the uncertainty in the axial placement of the sensor to $100 \mu m$. Since most measurements rely on differential measurements between sensing zones, the sensor's manufacturing error is used instead, which was taken to be $5 \mu m$.

The PETN used in these experiments was in the form of an ultrafine powder, an SEM of which is shown in Fig. 11. The small particle size means that it reliably initiates, since the surface has fewer deviations following pressing, and therefore more possible sites of initiation. A finer powder results in a smaller reaction time and shorter reaction zone[12]. Compared to other CHNO explosives such as TNT or TATB, PETN has a relatively small oxygen deficit. Therefore, compared to these other explosives, solid carbon forms less readily in the detonation products, with some thermodynamic stability analyses predicting that it does not form at all at low densities[13]. Since carbon is believed to cause the majority of electrical conductivity in the reaction zone[14], low density PETN provides a rigorous test for the performance of conductivity based sensors. A lesser degree of conductivity will nonetheless arise from ionisation, requiring greater diagnostic sensitivity.
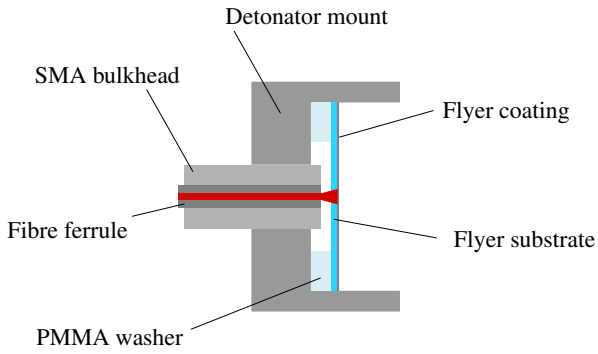
FIG. 9. The optical fibre is held by an SMA bulkhead inserted into the detonator mount. A PMMA washer separates the end of the fibre ferrule from the coated substrate. The PMMA cylinder containing the pressed PETN sits atop the flyer substrate, in the recess of the detonator mount.
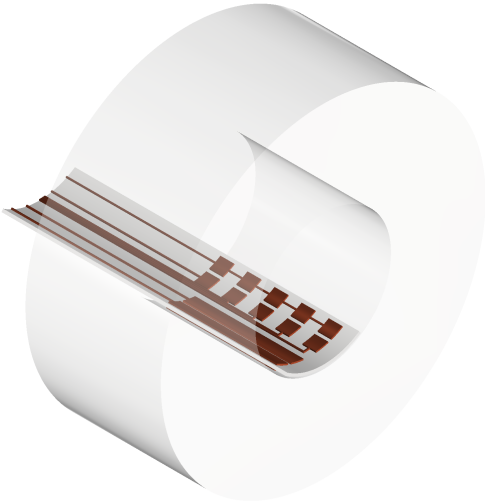

FIG. 10. The position of the sensor in the experiments, prior to pressing the PETN into the casing.
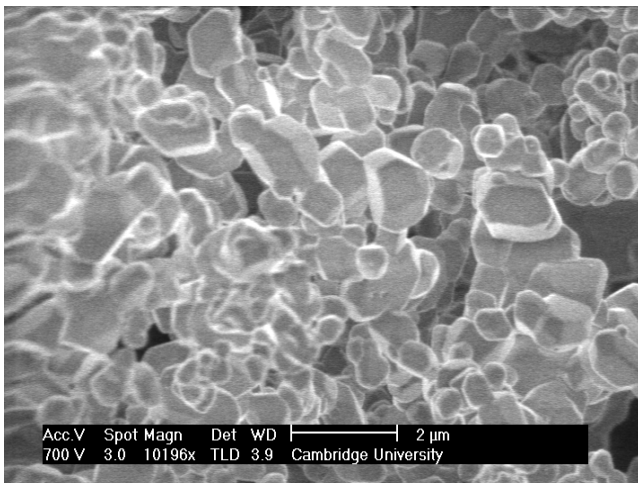

FIG. 11. Scanning electron microscope image of the ultrafine powder, which has an average particle size of 1 μm to 2 μm.

The powder was pressed into the casing using a a specially designed bidirectional floating piston press. The press has a free floating outer die containing two pistons and inner dies which can move axially relative to each other, but have relatively tight tolerances to reduce non-axial movement. The design exploits the principle that the friction between the wall and powder is transmitted better through denser powder. As pressure is applied to both pistons, the one which moves relative to the die is the one which faces least resistance from the powder, and therefore also the one at the less dense end. As each piston moves, the powder at its end densifies and resistance increases until it exceeds the force required to move the other piston. In this way the pistons alternately compress the powder in a way that reduces the effect of having a preferential pressing direction.

IV. RESULTS

The data gathered from each experiment consists of an oscilloscope trace for each channel covering the whole detonation event. An example of one channel's data is shown in Fig. 12 along with the processed misfit signal. Also shown is the mapping of the timing points on the misfit signal to the displacement-time plot in the style of Fig. 6.

A. Detonation Velocity

First, the detonation velocity at each density was calculated using the interval between timing points for the front of the conducting zone. As a proof of the technique's validity, the best approximation to the steady state velocity was calculated from the electrodes furthest from the initiation. These velocities are shown in Fig. 13 alongside literature data.

The calculated steady state detonation velocities are in reasonably close agreement with the literature values[15,16]. There is however some small discrepancy, which may be explained by differences in experimental setup – Dinegar [15] used a larger diameter charge. The diameter effect would be expected to increase the detonation velocity for larger diameters, hence the discrepancy at lower densities. At higher densities the experiments yield detonation velocities that are larger than those in[16]. Steady state velocity follows an approximately linear relationship with density over the range tested, although extrapolating this gradient would slightly overestimate the TMD detonation velocity – therefore the gradient is expected to flatten at higher densities. Since the apparatus was optimised for measuring the reaction zone and not velocities, the experimental error was large for these measurements.

B. Reaction Time

The calculated timing points also made it possible to calculate the width of the conductivity peak. There is a question of how closely the rise and fall in conductivity match the Von Neumann point and sonic point respectively – if they do
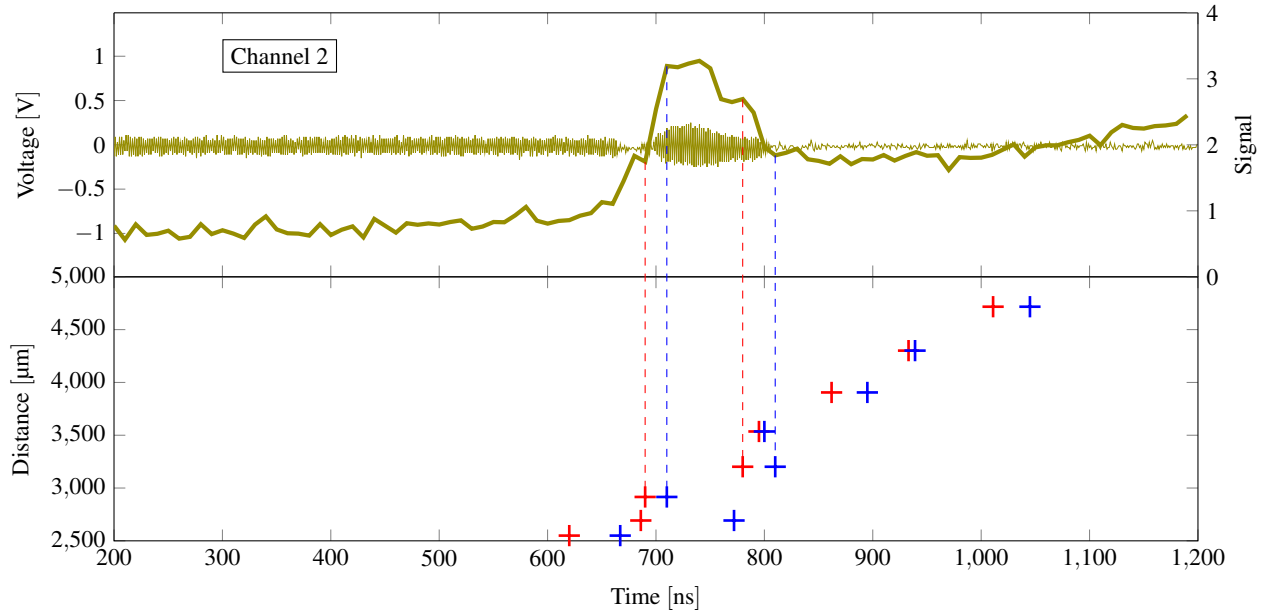
FIG. 12. Top are the raw data produced by one channel of the capacitive sensing system (thin line) and the transformed signal (thick line). Bottom is the displacement-time plot derived from this channel and the others, with the dashed lines showing the timing points for this channel. This series is ultrafine PETN at $1.05\,\mathrm{g\,cm^{-3}}$. In this case there are points where the sonic points appear out of place – this is discussed below.
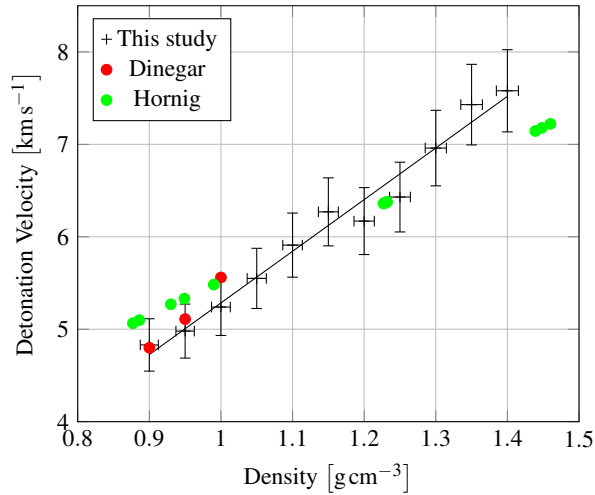

FIG. 13. The detonation velocities measured using the last sensing zone of the capacitive sensors. Also shown are values from Dinegar[15] and Hornig[16]. The experimental results differ from those of Hornig[16] at higher densities.
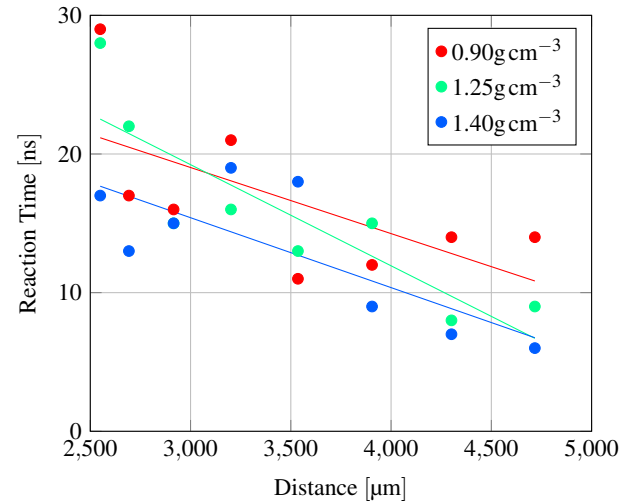

FIG. 14. The reaction time progression for selected densities. The reaction times are mostly between $10\,\mathrm{ns}$ to $20\,\mathrm{ns}$ with a weak tendency to decrease with distance from the initiation point, and also with density.

match then the length of the conductivity zone is a good proxy for the reaction zone length. This matter was discussed by Ershov *et al.*[17], who found strong correlation between the width of the main conductivity peak and the reaction zone length as measured by optical methods. They also found a distinct long tail of lower conductivity behind the main peak, which decreased with distance and corresponds to the rarefaction wave. The conductivity of this tail was attributed not to reaction but to the presence of solid carbon which oxidises or disperses

at a relatively slow rate. Due to PETN's small negative oxygen balance the formation of this solid carbon is believed to be minimal, especially at low densities. With the assumption that the conduction zone can be equated with the reaction zone, the reaction times for several densities and distances are shown in Fig. 14.

The reaction time data is quite sensitive to the anomalous results, since the limited supply of material only permitted a single shot to be performed for each density. However there
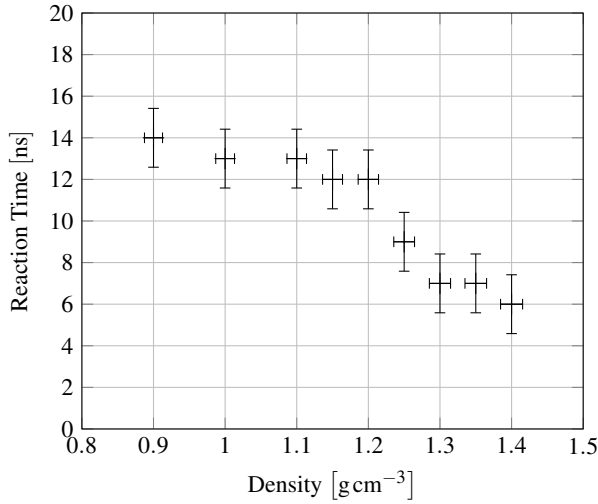
FIG. 15. The final reaction time vs. density. Denser pressings exhibit shorter steady state reaction times, particularly above $1.10\,\mathrm{g\,cm^{-3}}$.
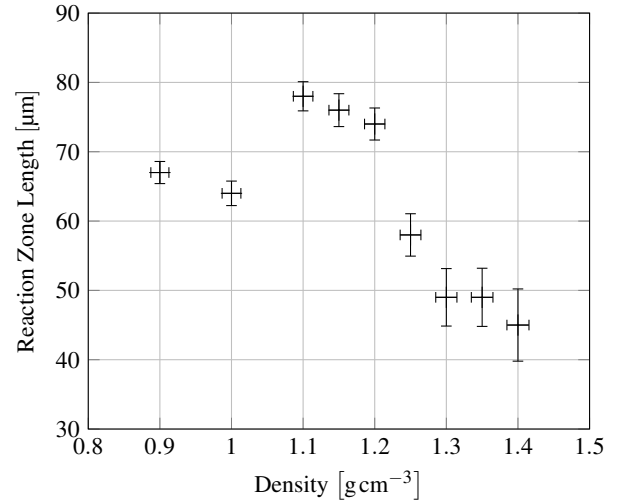

FIG. 16. The final reaction zone length vs. density. The reaction zone length is greatest at $1.10\,\mathrm{g\,cm^{-3}}$, and decreases with density above this value. For the lowest densities, the smaller detonation velocity results in a smaller reaction zone length.

is a general trend for the reaction time to decrease as the detonation moves through the charge.

The reaction time also has a density dependence – the steady state is around $14\,\mathrm{ns}$ at $0.90\,\mathrm{g\,cm^{-3}}$ while at $1.40\,\mathrm{g\,cm^{-3}}$ it is around $6\,\mathrm{ns}$. Most of the variation in reaction time with respect to density occurs above $1.10\,\mathrm{g\,cm^{-3}}$, whereas below this density there is very little variation. Utkin *et al.* [5] found a reaction time of $50\,\mathrm{ns}$ using $\sim500\,\mathrm{\mu m}$ particles, suggesting a dependence on particle size. Other studies[14,18] found values closer to the ones here, but did not specify the particle size. Fig. 15 shows the steady state (at the farthest electrode) reaction time for the different densities.

An explanation for the anomalous points where the reaction time is larger than expected may lie in the assumption made about the equivalence between the conduction zone and the reaction zone. As can be seen from Fig. 12, the misfit signal rise due to the detonation front is greater than the fall that occurs over the rarefaction tail. Therefore the uncertainty in determining the rear of the reaction zone is greater than the uncertainty in determining the front. The conductivity of the reaction zone is more similar to the conductivity of the rarefaction tail than it is to the conductivity of the unreacted explosive, therefore it is harder to identify the sonic point than the shock. A sonic point misattributed to somewhere in the rarefaction tail would cause an anomalously large reaction time.

C. Reaction Zone Length

By combining the timing points with the velocity profiles according to the relationships in Table. I, we derive the reaction zone length ξ. The best approximation to the steady state lengths calculated from the farthest electrodes are shown in Fig. 16.

As with the reaction times there is a decreasing trend for densities higher than $1.10\,\mathrm{g\,cm^{-3}}$, however for lower densities the reaction zone is also shorter. This behaviour is a consequence of the trends exhibited by both detonation velocity and reaction time. While the reaction time is greater at lower densities, the detonation velocity is smaller. Below $1.10\,\mathrm{g\,cm^{-3}}$ the smaller detonation velocity is more important, so the reaction zone length is smaller. As the density is increased up to $1.10\,\mathrm{g\,cm^{-3}}$ the reaction time trend becomes more important, and the detonation velocity trend becomes less important.

At higher densities the gradient of the detonation velocity with respect to density decreases (Fig. 13) while the gradient of the reaction time with respect to density increases (Fig. 15). The reaction zone length therefore decreases with increasing density above $1.10\,\mathrm{g\,cm^{-3}}$.

The reaction zone length progressions are shown in Fig. 17. They exhibit the same trend as the reaction times of decreasing with distance from the initiation site, albeit with a gentler approach to steady state. The smaller slope is due to the end of the ramping up phase of the detonation velocity having an opposing effect to the decrease in reaction time.

Most literature deals with reaction zone time, so the comparison with these results is the same as discussed above, since the detonation velocity is well-documented. Lubyatinsky and Loboiko [19] measured reaction zone lengths of less than $30\,\mathrm{\mu m}$ in agatised PETN, close to TMD, but the non-agatised samples had much longer reaction zone lengths. The difference was explained as being due to the non-planarity of the shock causing slower compression and reaction in some crystals. That the results here were closer to the agatised samples suggests that the ultrafine powder supports a relatively planar shock.

The higher density effect is expected, and agrees with literature[18], however the decreasing reaction zone length with density at lower densities is somewhat unexpected. From Fig. 17 it can be seen that this behaviour only takes hold a few millimetres into the detonation, which reflects the varia-
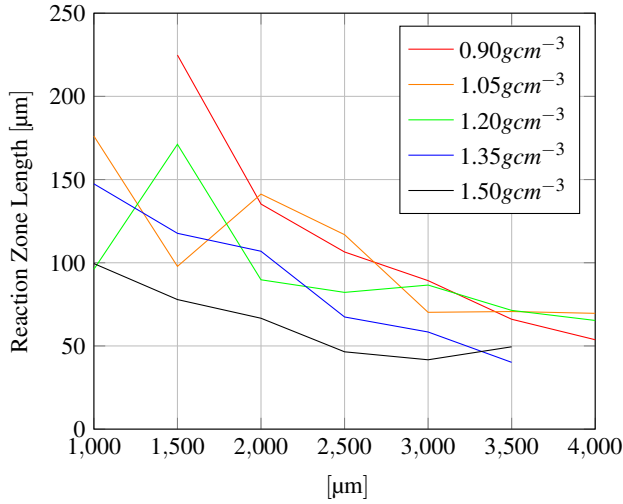
FIG. 17. The progression of the reaction zone length for a range of densities. There is a trend for reaction zone length to decrease with distance for each density. As with the density experiments, the steady state reaction zone length peaks at an intermediate density $(1.05\,\mathrm{g\,cm^{-3}})$. The initial reaction zone lengths are especially large at lower densities, and exhibit a greater variation.

TABLE II. Summary of the results from the density study, showing the (steady) detonation velocity (D), reaction time (τ) and reaction zone length (ξ). Also shown is the calculated lost time. Suspected anomalous results are enclosed by parentheses.

$\rho/\mathrm{g\,cm^{-3}}$	$D/\mathrm{km\,s^{-1}}$	τ/ns	$\xi/\mathrm{\mu m}$	t_L/ns
0.90	4.83	14	67	670
0.95	4.98	(32)	(146)	630
1.00	5.24	13	64	500
1.05	5.55	(34)	(185)	440
1.10	5.91	13	78	380
1.15	6.27	12	76	320
1.20	6.17	12	74	250
1.25	6.43	9	58	250
1.30	6.96	7	49	180
1.35	7.43	7	49	200
1.40	7.58	6	45	150

tion in early reaction time being comparatively larger than the variation in early detonation velocity.

V. DISCUSSION

In the density experiments the detonation velocity ramped up from a smaller value to the final steady state value. This behaviour is likely due to the detonation wave overtaking a precursor shock. The precursor desensitises the explosive by collapsing voids and releasing stress, so the reaction is slower until the detonation overtakes the precursor, at which point it accelerates to steady state.

The differing shock impedance of samples results in a higher pressure in the denser samples in response to identi-
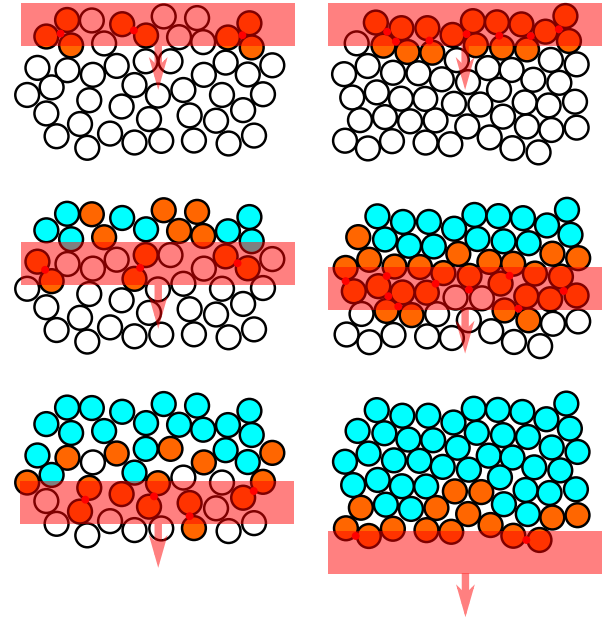

FIG. 18. Illustration of why denser pressings have shorter reaction times. As the shock (pink) passes through, more critical hot spots (red) are formed in the denser bed (right) since there are more voids and points of contact. Practically all potential hot spots become critical due to the high pressure. Therefore more grains in each layer begin to react (orange). Grains not in proximity to a hot spot can only start to burn later – there are more of these in the lower density bed (left). The former positions of grains that are fully reacted are marked in blue. For low densities, at any given point along the detonation direction, there will be more time before all the grains at that point have completely reacted.

cal flyers. However, this pressure is large enough such that practically all potential hot spots will be above the critical hot spot size. The limiting factor is therefore hot spot growth.

The reaction time exhibits a dependence on density, with a shorter reaction time being seen at higher densities. At higher densities the powder will have smaller and more numerous voids, and more points of contact between particles. There will therefore be more potential sites for hot spot ignition, which will almost all spontaneously grow due to the high pressure. If there are more hot spots, then more particles will start chemical reaction sooner. Grains which do not start reacting will have to wait for jetting, impact or heat conduction from already burning grains before they start burning. Since the reaction time is determined by the time for surface burning to reach the centre of the particles, if a greater fraction of particles start reaction sooner, then less time will have elapse before the reaction is complete. This argument is illustrated in Fig. 18.

Across all densities, the reaction time was greater closer to the source of initiation before settling down to a shorter steady state value. The most likely explanation for this relationship is that the material compacts as the detonation passes through. The above arguments concerning the dependence on density then also apply to the dependence on distance, since increasing densification occurs with distance. There may also

be heat conduction through the porous material, which could increase the reaction rate, but it is unlikely that this happens fast enough compared to the other mechanisms by which the reaction is transferred from one particle to another.

It is important to make the distinction between the Lagrangian and Eulerian frames of reference, and which frame is applicable for each measurement. In the Lagrangian frame, the sensor moves along with the material, so the reaction time can be associated with a particular fluid element. In the Eulerian frame, the fluid moves past the sensor as it reacts, therefore the observed reaction time will be shorter since the reacting material is in the sensing zone for less time. The reference frame argument is a possible alternative explanation for why the reaction time was initially larger before shrinking. If the sensor initially moved along with the material, but was then overtaken or arrested, then the frame would shift from Lagrangian to Eulerian. It is not believed that this occurred, however, since there was no initial increase in reaction time, which would have occurred had the sensor started moving with the material.

The explanations for the dependence of the reaction time on density and distance carry over to the reaction zone length, although the calculation of this quantity also requires the detonation velocity. Detonation velocity increases with density, while reaction time decreases, so there is a trade-off in the reaction zone length. The reaction time trend becomes more important at higher densities, and the detonation velocity trend at lower densities. The steady state reaction zone length was greatest at an intermediate density – $1.10 \, \mathrm{g \, cm^{-3}}$.

In contrast, the reaction time variation with distance is large enough that the ramping up of velocity does not overrule it for any of the experiments performed here. However, the reaction zone length does take longer to reach a steady value than the reaction time, most likely due to this effect.

The causal chain of events that explain these relationships is summarised as follows:

1. The flyer hits the surface of the bed at the same velocity regardless of the material properties. A higher pressure shock is imparted to the higher densities. In all cases the shock is short, and rapidly subsumed by the release wave from the rear of the flyer. Lateral release waves do not significantly affect the size of the shocked region.

2. There is little delay to detonation commencing in all cases. Run to detonation is longer for the denser beds, but due to the strength of the shock it occurs over a much shorter timescale than the other processes at work.

3. Higher density pressings have more (albeit smaller) voids and points of contact in the shocked region, therefore there are more sites for hot spot formation. Due to the high pressure imparted, the hot spots that form are larger than the critical size, and grow spontaneously.

4. A greater proportion of particles start burning promptly, and therefore also finish burning earlier. Therefore the reaction time is shorter, while the reaction zone length

depends on both the reaction time and detonation velocity.

5. Densification of the bed causes the reaction time to decrease with distance from initiation to a steady state value.

6. The ramping up of the detonation velocity combined with the decreasing reaction time combine to produce a reaction zone length that decreases at a gentle rate. At higher densities the slope is smaller than at lower densities.

7. The opposite trends in velocity and reaction time result in an intermediate density where the reaction zone length is greatest.

VI. CONCLUSIONS

A novel diagnostic based on capacitive sensing has been developed which exploits the response of a high frequency signal passed through a sensor to a conducting object or region in its proximity. The signal is processed by applying a continuous wavelet transform to the signal and comparing its misfit with a baseline. The design of the circuit amplified the size of this effect relative to background noise. Active shielding was used to reduce stray capacitance and coaxial lines reduced external noise.

Capacitive sensing was applied to small cylindrical pellets of ultrafine PETN. Analysis based on the rises and falls of the processed signal was performed to convert the data into displacement-time plots of the front and rear of the reaction zone, from which the detonation velocity, reaction time and reaction zone length could be found. The method was sufficiently sensitive to detect the relatively weakly conducting reaction zone of PETN, and sufficiently fast to resolve its edges. Unlike other electromagnetic diagnostics, it does not require high voltages or embedding within the sample, since the data is obtained from changes in the electric field rather than the current.

Detonation velocities were in close agreement with those found by previous work across a range of different densities, supporting the validity of the method. The reaction time was found to depend on the density of the pressing: the steady value ranged from 14 ns at $0.90 \, \mathrm{g \, cm^{-3}}$ to 6 ns at $1.40 \, \mathrm{g \, cm^{-3}}$. It is believed that denser pressings will form a greater number of critical hot spots in any given layer, so more grains in that layer will start burning together (and therefore also finish burning together). The reaction time also decreased with distance, possibly suggesting the presence of a precursor compaction wave that increases the density as it moves through the bed, decreasing the reaction time. The reaction times found were similar to the literature values, although these have more variation (from 'less than 10 ns'[14] to 50 ns[5]).

The reaction zone length's dependence on density inherits the dependence of the detonation velocity and the reaction time. For densities below about $1.10 \, \mathrm{g \, cm^{-3}}$ the slower detonation velocity means the reaction zone length shrinks

with decreasing density, despite the reaction time increasing. Above this density the reaction zone length follows the same decreasing trend as the reaction time, albeit tempered by the increasing detonation velocity. The steady reaction zone lengths measured ranged from $67\,\mu m$ at $0.90\,g\,cm^{-3}$ to $45\,\mu m$ at $1.40\,g\,cm^{-3}$, with a peak of $78\,\mu m$ at $1.10\,g\,cm^{-3}$. Similar values were found when the sensor was oriented perpendicular to the axis.

The experiments performed using the capacitive sensors have given new insights into the evolution of the reaction zone and its dependence on density. While previous studies have measured the reaction zone at steady state, they have not shown its transitory behaviour from initiation, nor have they examined as broad a range of densities as has been done here. The technique described here may be applicable to wider work within the field of energetic materials.

DATA AVAILABILITY STATEMENT

Data are available from the authors upon reasonable request and with the permission of AWE.

[1] B. Hayes, "Electrical measurements in reaction zones of high explosives," in *Symposium (International) on Combustion*, Vol. 10 (Elsevier, 1965) pp. 869–874.

[2] D. Tasker, R. Lee, and P. Gustavson, "The measurement of electrical conductivity in detonating condensed explosives," Tech. Rep. (NAVAL SURFACE WARFARE CENTER DAHLGREN DIV VA, 1993).

[3] A. Ershov, P. Zubkov, and L. Luk'yanchikov, "Measurements of the electrical conductivity profile in the detonation front of solid explosives," Combustion, Explosion and Shock Waves **10**, 776–782 (1974).

[4] A. Frank, H. Chau, R. Lee, P. Vitello, and P. Souers, "Reaction zones in ultrafine TATB," Propell. Explos. Pyrotech. **28**, 259–264 (2003).

[5] A. Utkin, V. Mochalova, A. Rogacheva, and V. Yakushev, "Structure of detonation waves in PETN," Combustion, Explosion, and Shock Waves **53**, 199–204 (2017).

[6] A. Romani, N. Manaresi, L. Marzocchi, G. Medoro, A. Leonardi, L. Altomare, M. Tartagni, and R. Guerrieri, "Capacitive sensor array for localization of bioparticles in CMOS lab-on-a-chip," in *2004 IEEE International Solid-State Circuits Conference (IEEE Cat. No. 04CH37519)* (IEEE, 2004) pp. 224–225.

[7] S. Guha, K. Schmalz, C. Wenger, and F. Herzel, "Self-calibrating highly sensitive dynamic capacitance sensor: towards rapid sensing and counting of particles in laminar flow systems," Analyst **140**, 3262–3272 (2015).

[8] Tektronix, "XYZs of oscilloscope," (2001).

[9] D. Wang, "Capacitive sensing: Ins and outs of active shielding," Texas Instruments, Application report SNOA926A–February (2015).

[10] A. Grossmann, R. Kronland-Martinet, and J. Morlet, "Reading and understanding continuous wavelet transforms," in *Wavelets* (Springer, 1990) pp. 2–20.

[11] M. Kristeková, J. Kristek, and P. Moczo, "Time-frequency misfit and goodness-of-fit criteria for quantitative comparison of time signals," Geophysical Journal International **178**, 813–825 (2009).

[12] D. Price, A. Clairmont Jr, and I. Jaffe, "Explosive behaviour of ammonium perchlorate," Combustion and Flame **11**, 415–425 (1967).

[13] F. H. Ree, "A statistical mechanical theory of chemically reacting multiphase mixtures: Application to the detonation properties of petn," The Journal of chemical physics **81**, 1251–1263 (1984).

[14] C. Tarver, "Detonation reaction zones in condensed explosives," in *Shock Compression of Condensed Matter - 2005*, edited by M. Furnish, M. Elert, T. Russell, and C. White (American Institute of Physics, Melville, NY, 2006) pp. 1026–1029.

[15] R. Dinegar, "Detonation velocity of PETN in small confined cylindrical charges," Propell. Explos. **1**, 97–100 (1976).

[16] H. Hornig, "Equation of state of detonation products," in *5th Symposium (International) on Detonation, 1970* (1970) pp. 503–511.

[17] A. Ershov, N. Satonkina, A. Plastinin, and A. Yunoshev, "Diagnostics of the chemical reaction zone in detonation of solid explosives," Combustion, Explosion, and Shock Waves **56**, 705–715 (2020).

[18] B. Loboiko and S. Lubyatinsky, "Reaction zones of detonating solid explosives," Combust. Explos. Shock Waves **36**, 716–733 (2000).

[19] S. Lubyatinsky and B. Loboiko, "Density effect on detonation reaction zone length in solid explosives," in *Shock Compression of Condensed Matter - 1997*, edited by S. Schmidt, D. Dandekar, and J. Forbes (American Institute of Physics, Woodbury, New York, 1998) pp. 743–746.